Available online at www.sciencedirect.com
ScienceDirect
Trans. Nonferrous Met. Soc. China 33(2023) 1425−1436
Transactions of Nonferrous Metals Society of China
www.tnmsc.cn

# Mechanical properties and deformation behaviors of Ti−5Al−5Mo−1Fe−1Cr alloy with duplex and single-phase microstructures

Chao-qiang LIU[1], Zong-yu XIE[1], Xiao-yong ZHANG[1], Hong-ge YAN[2], Ke-chao ZHOU[1], Min SONG[1]

1. State Key Laboratory of Powder Metallurgy, Central South University, Changsha 410083, China;
2. College of Materials Science and Engineering, Hunan University, Changsha 410082, China

Received 17 November 2021; accepted 1 March 2022

**Abstract:** To clarify the differences of mechanical properties and deformation behaviors of a Ti−5Al−5Mo−1Fe−1Cr (wt.%) alloy with duplex and single-phase microstructures, the tensile properties and deformation modes of the alloy with these two different microstructures were studied systematically. The results show that the sample with the duplex microstructure has a tensile yield strength of 886 MPa, an ultimate tensile strength of 1075 MPa and an elongation of 21.5%. The sample with the single $\beta$ phase has a relatively lower strength and a similar elongation. The sample with the duplex microstructure has a ductile fracture mode and deforms via dislocation slipping in the $\beta$ matrix and spherical or plate-like $\alpha$ phases. The slip systems are $\{112\}_\beta\langle 11\bar{1}\rangle_\beta$ in $\beta$ matrix, and $\{11\bar{2}2\}_\alpha\langle 11\bar{2}\bar{3}\rangle_\alpha$ and $\{10\bar{1}0\}_\alpha\langle 1\bar{2}10\rangle_\alpha$ in $\alpha$ phase. In contrast, the single-phase sample has a quasi-cleavage fracture mode and deforms via dislocation slipping and stress-induced $\alpha''$ martensite transformation, and the slip systems are $\{110\}_\beta\langle 1\bar{1}1\rangle_\beta$ and $\{112\}_\beta\langle 11\bar{1}\rangle_\beta$.

**Key words:** near $\beta$-Ti alloys; mechanical properties; deformation behavior; dislocation slipping; stress-induced martensite transformation

## 1 Introduction

Titanium alloys have received considerable attention in industrial and academic communities since they have excellent mechanical properties, such as corrosion resistance, biocompatibility, etc., and complicated and representative microstructures [1−4]. The mechanical properties of titanium alloys are the decisive factor for their applications in aerospace industry and are closely related to the composition and microstructure of the alloys [5−8]. Tuning the morphology and distribution of $\alpha$ and $\beta$ phases [9−12] and changing the stability of $\beta$ phase [13] significantly affect the strength, plasticity and strain hardening rate of the alloys. Since the plasticity and strain hardening rate of the alloys strongly depend on the deformation behavior of the microstructure [14−17], studying the deformation behavior of different microstructures in titanium alloys is very important in terms of the development of titanium alloys with high strength and toughness.

Duplex microstructure is a kind of typical microstructure in titanium alloys [18]. It consists of plate-like and spherical $\alpha$ phase in the $\beta$ matrix. In general, the titanium alloys with this kind of microstructure have a good comprehensive mechanical property, since the plate-like $\alpha$ phase can effectively impede dislocation movement, leading to the high strength, and the spherical $\alpha$ phase itself can deform plastically, contributing to the large plasticity [7,10]. It has been reported that the plastic deformation of the spherical $\alpha$ phase is

**Corresponding author:** Min SONG, Tel: +86-731-88877677, E-mail: msong@csu.edu.cn
DOI: 10.1016/S1003-6326(23)66193-X

achieved via dislocation slipping or twining [10,14]. So far, $\{10\bar{1}1\}$ and $\{10\bar{1}2\}$ twins have been observed in the deformed spherical $\alpha$ phase [14,19].

Single $\beta$ phase microstructure is another kind of commonly observed microstructure in titanium alloys [20−22]. It is generally acquired by initial solution treatment in $\beta$ phase region and then quenching to the room temperature in metastable $\beta$ titanium alloys with a relatively high $\beta$-stabilizer content [23]. The deformation behavior in single $\beta$ phase microstructure involves reportedly stress-induced martensite transformation, deformation twinning and dislocation slipping [24−26]. The stress-induced phase transformation and deformation twinning are received increased attention in recent years [27−30], as their occurrence can make the alloys withstand large plastic deformation before fracture, and they are known as transformation-induced plasticity (TRIP) and twinning-induced plasticity (TWIP) effects [22,27]. It has been reported that the phases induced by stress include $\alpha''$ and/or $\omega$, and the twins generated during deformation are $\{332\}_\beta$ and $\{112\}_\beta$ twins in titanium alloys with single $\beta$ phase microstructure [29−31].

Although it is well known that dislocation slipping is a kind of vital deformation mode for both duplex and single $\beta$ phase microstructures in titanium alloys, the systematic study on dislocation slipping is less, and which slip system can be activated during deformation remains unclear, especially in some recently designed alloys. It has been suggested that the slipping plane of the dislocations in metal materials could be straightforward given through the combined analysis of slip traces and the corresponding pole figures, and the slip system could be consequently acquired [32]. This technique has been widely utilized to analyze the slip system in magnesium alloys [32−34].

Ti−5Al−5Mo−1Fe−1Cr alloy is a kind of our recently designed near-$\beta$ titanium alloy. This alloy does not include expensive V element compared to the commercial TC18 alloy and is a low-cost titanium alloy. In order to promote its development, it is necessary to investigate the mechanical properties of this alloy with two kinds of typical microstructures, namely duplex and single $\beta$ phase microstructures.

Therefore, in the present study, we firstly prepared the duplex and single $\beta$ phase microstructures in Ti−5Al−5Mo−1Fe−1Cr alloy, by solution treatment at different temperatures and then systematically investigated the mechanical properties and deformation behaviors of the alloy with different microstructures. By the combined analysis of slip traces and pole figures, the slip systems in $\alpha$ phase and $\beta$ matrix in the duplex microstructure and the slip systems in the single $\beta$ microstructure were determined. Our findings are useful to a deeper understanding of the deformation behaviors in titanium alloys and could also facilitate the development of new titanium alloys.

## 2 Experimental

An alloy with a nominal composition of Ti−5Al−5Mo−1Fe−1Cr (wt.%) was prepared by vacuum arc melting and then forged three times into a bar with a diameter of 120 mm. The $\alpha/\beta$-transus temperature of the alloy was estimated to be 873 °C according to differential scanning calorimetry analysis. Small samples cut from the forged bar were divided into two groups. One of them was solution-treated at 800 °C for 1 h, followed by air cooling, and samples in this group are designated as 800AC. Samples in another group were solution-treated at 950 °C for 1 h, followed by air cooling, and designated as 950AC. To avoid the influence of oxidation, the thickness of the solution-treated samples was decreased by 1.5 mm via polishing. Tension and compression tests were conducted on an Instron−3369 machine at room temperature. The tensile specimens have a gauge length of 24 mm and a cross section of 6 mm × 3 mm. To ensure the validity of the tensile data, three samples in the same condition were tested. Hardness pits were fabricated using a BUEHLER−5104 Vickers hardness tester to roughly examine the deformation behaviors of samples.

The phase constitutions in 800AC and 950AC samples were analyzed by a D/MAX−3C X-ray diffractometer (XRD). Leica DM4000M optical microscope (OM) was employed to examine the deformed microstructures around the hardness pits. To systematically characterize the deformation behaviors of the 800AC and 950AC samples, they were compressed by 6% and the deformed microstructures were characterized by electron microscopy. Secondary electron (SE), backscattered

electron (BSE) and electron backscattered diffraction (EBSD) characterizations were carried out in a Nova Nano SEM 320 scanning electron microscope (SEM) equipped with energy dispersive X-ray spectrometer (EDS). Samples for SEM and EBSD characterizations were prepared by mechanically grinding and then electro-polishing in a solution composed of 5 vol.% $HClO_4$, 35 vol.% $CH_3(CH_2)_3OH$, and 60 vol.% $CH_3OH$ at −30 °C.

## 3 Results and discussion

### 3.1 Initial microstructures

Figure 1 shows the XRD patterns of the 800AC and 950AC samples. The XRD pattern of the 800AC sample includes $\alpha$ and $\beta$ diffraction peaks simultaneously, while that of the 950AC sample includes exclusively $\beta$ diffraction peaks. This indicates that the 800AC sample includes $\alpha$ and $\beta$ phases, yet the 950AC sample only includes $\beta$ phase. Figures 2(a) and (b) show the BSE images of 800AC and 950AC samples, respectively. Spherical and plate-like $\alpha$ particles are observed in the 800AC sample. The diameters of the spherical $\alpha$ particles are in a range of 5−10 μm, and the $\alpha$ plates have a length of 3−10 μm and a width of 1−2 μm. For the 950AC sample, there is no secondary phase being detected and the $\beta$ phase is completely retained after being quenched in the air, as shown in Fig. 2(b). The grain size of the $\beta$ matrix is measured to be 150−300 μm. Figures 2(c) and (d) show an enlarged BSE image of the 800AC sample and the corresponding compositional results of the $\alpha$ and $\beta$ phases, respectively. Al element distributes mainly in the $\alpha$ phase, and Mo, Cr and Fe elements distribute mostly in the $\beta$ phase. This is expected since Al is a typical $\alpha$-stabilizer, and Mo, Cr and Fe are typical $\beta$-stabilizers [23]. Considering that these alloying elements are expected to distribute uniformly in the 950AC sample where there is no $\alpha$ phase, therefore, presence of the $\alpha$ phase could cause re-distribution of alloying elements in the alloy.

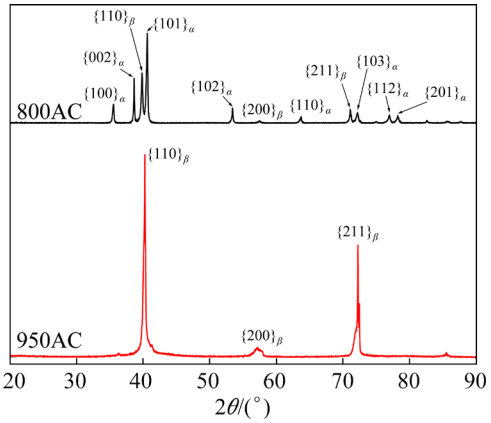


**Fig. 1** XRD patterns of 800AC and 950AC samples

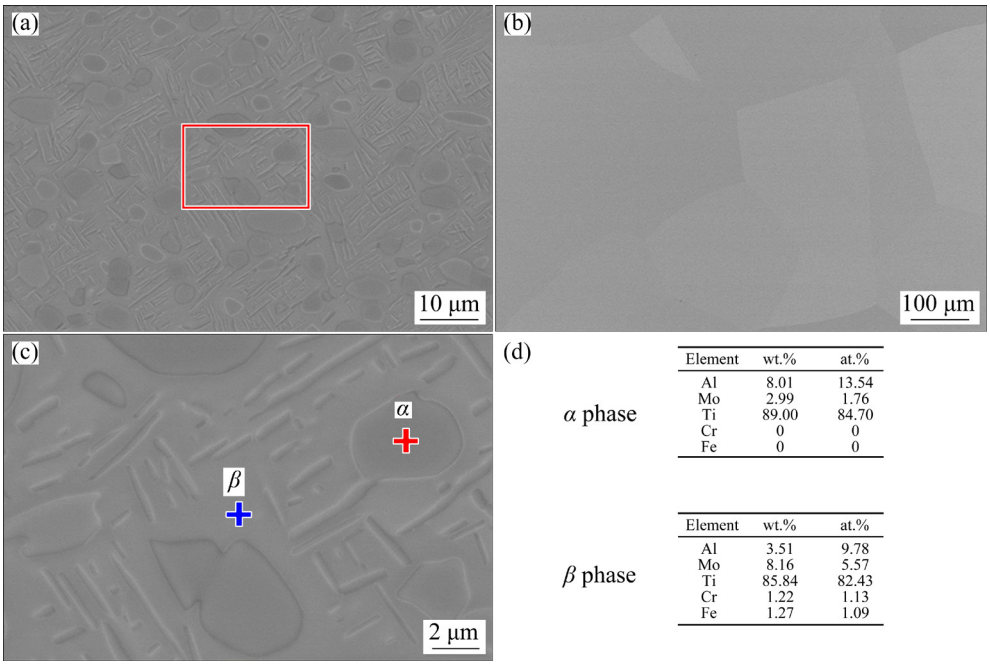


**Fig. 2** BSE images showing duplex and single phase microstructures in 800AC (a) and 950AC (b) samples, respectively, enlarged image (c) of region marked by red frame in (a), and SEM−EDS compositional results (d) of $\alpha$ and $\beta$ phases in (c)

### 3.2 Mechanical properties and fracture modes

Figure 3(a) shows the tensile true stress−strain curves of 800AC and 950AC samples. The 800AC sample has a tensile yield strength (TYS) of 886 MPa, an ultimate tensile strength (UTS) of 1075 MPa, and an elongation of 21.5%. The 950AC sample has a lower strength but a similar elongation. Its TYS and UTS are 760 MPa and 866 MPa, respectively, and its elongation is 22.5%. This is expected as the 800AC sample includes lots of $\alpha$ phases that can strengthen the alloy. Careful comparison of the true stress−strain curves of these two samples reveals that the 800AC sample has an obvious stress decline stage after its UTS is reached. Figure 3(b) shows the curves of the strain hardening rate of these two samples. The 800AC sample has a higher strain hardening rate in the stage of uniform plastic deformation. Figures 3(c, d) show the macroscopic photographs of the fractured 800AC and 950AC samples, respectively. Necking can be detected in the fractured 800AC sample, while it is invisible in the fractured 950AC sample.

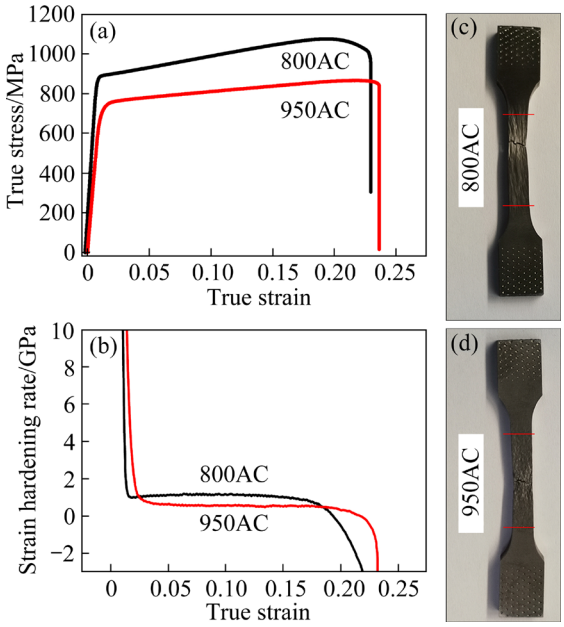


**Fig. 3** Tensile true stress−strain curves (a) and strain hardening rate curves (b) of 800AC and 950AC samples, and macroscopic photographs of fractured 800AC (c) and 950AC (d) samples

Figure 4 shows the fractographs of the 800AC and 950AC samples. The fracture microstructure of the 800AC sample is dominated by dimples, which implies that the fracture mode of the 800AC sample is ductile fracture. This explains exactly the occurrence of necking during tensile test in the

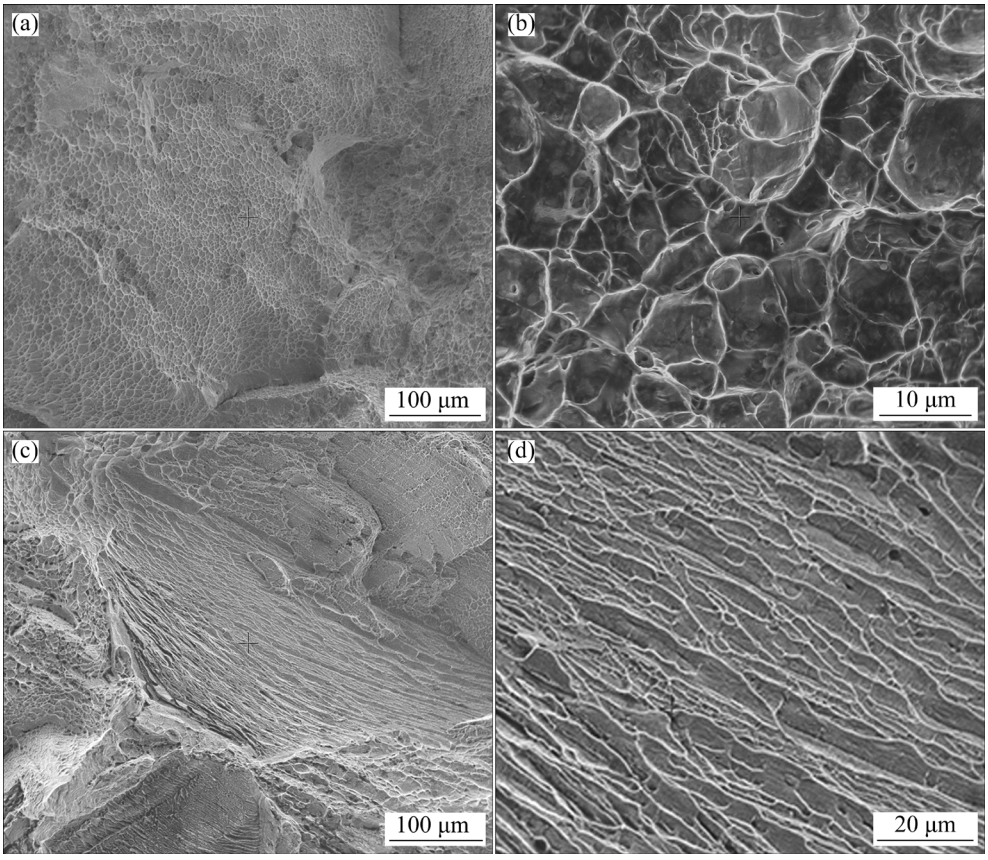


**Fig. 4** Low-magnification (a, c) and high-magnification (b, d) fractographs of 800AC (a, b) and 950AC (c, d) samples

800AC sample. As the developing of dimples in the metal materials usually weakens the materials, the formation of the dimples would result in the decrease of the strength. This rationalizes the presence of stress decline stage in the true stress−strain curve of the 800AC sample. In contrast, the 950AC sample has a completely different fracture microstructure. Torn edges and cleavage faces dominate the fracture microstructure except that some shallow dimples are occasionally detected. This kind of fracture microstructure implies that the fracture mode for the 950AC sample is quasi-cleavage fracture, which explains why there is no necking in the sample during tensile test (Fig. 3(d)).

### 3.3 Deformation behaviors

Even though the 800AC and 950AC samples have different fracture modes, they have almost the same elongations. In order to understand the origin of their elongation similarity, it is necessary to systematically investigate the deformation behaviors of the 800AC and 950AC samples. To preliminary study their deformation behaviors, we firstly made hardness pits on the polished surfaces of the two samples and then observed the deformed microstructures around the pits. This method was used to study the deformation behavior of alloys in literature [35]. Figures 5(a) and (c) show the OM images of two hardness pits on the polished surface of the 800AC specimen, and the loading forces for the pits are 50 and 300 N, respectively. Slip traces can be detected around the pits, as marked by red dashed circles. Figure 5(b) shows an enlarged image of a region located at the left top corner of the pit in Fig. 5(a). The slip traces are relatively weak and only observed in $\beta$ matrix, i.e., they do not cross the spherical $\alpha$ particles. This indicates that the dislocation movement has been inhibited by the $\alpha$ particles. The largest distance between the slip trace and the pit is about 50 μm, indicating that plastic deformation could extend 50 μm when the loading force is 50 N. When the loading force is increased to 300 N, there are more slip traces around the hardness pit and they are more obvious, as shown in Figs. 5(c) and (d), indicating that a severer plastic deformation occurs around the pit. In addition, some slip traces can intersect the spherical

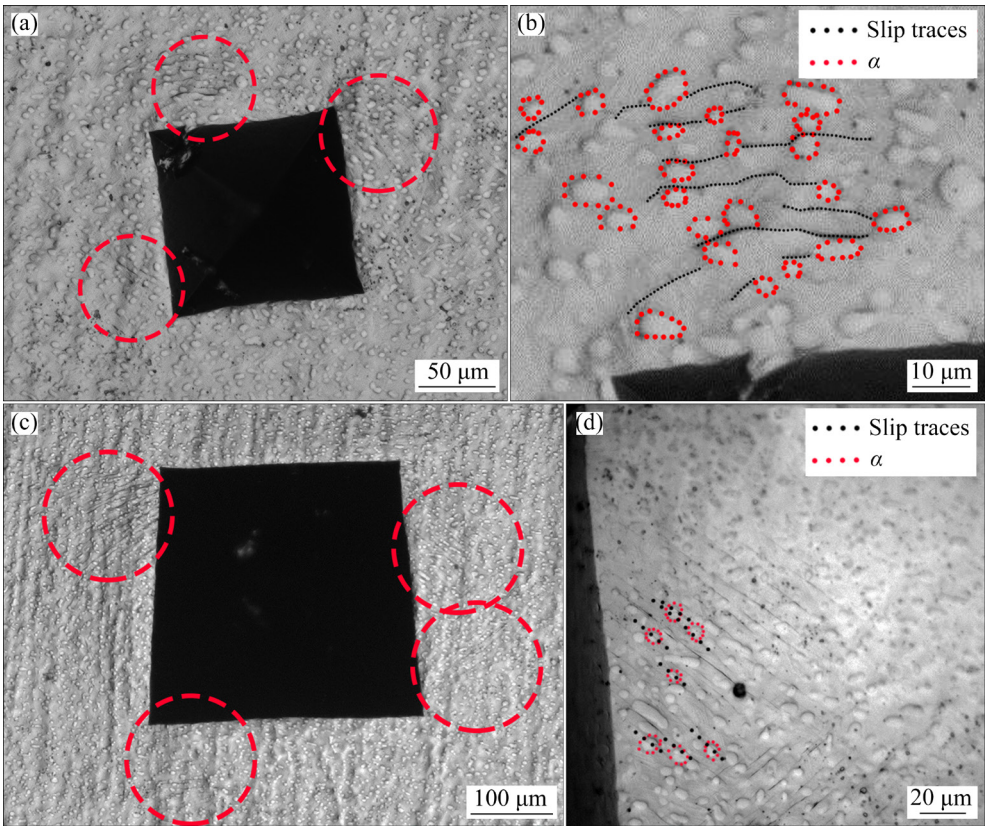


**Fig. 5** OM images (a, c) showing slip traces around two different pits generated by hardness tester in 800AC sample at loading forces of 50 N (a) and 300 N (c), and enlarged images (b, d) of areas immediately adjacent to spits in (a) and (c), respectively (Red dashed circles mark some regions having obvious slip traces)

$\alpha$ particles, suggesting that dislocations can cross the interfaces between the spherical $\alpha$ particles and $\beta$ matrix with the increase in the degree of the plastic deformation. The farthest slip trace from the pit is approximately 100 μm, indicating that the plastic deformation has a larger extending distance in this case.

Figure 6(a) shows the OM image of hardness pit at a loading force of 50 N on the polished surface of a 950AC sample. Similarly, slip traces can be observed around the pit, as marked by red dashed circles. Figure 6(b) shows an enlarged image of a region located at the left bottom corner of the pit. Some of slip traces are curving, and some of them are very straight and parallel to each other. These slip traces end on the grain boundaries (GBs), suggesting that dislocation movement has been blocked by the GBs. When the loading force is increased to 300 N, more slip traces are detected, as shown in Fig. 6(c). Figure 6(d) shows an enlarged image at the left top corner of the pit. Interestingly, some slip traces across the GBs are visible in this case. These traces are connected to the GBs and their distributions and morphologies are different from those adjacent to the pit, implying that different dislocations might be activated from the GBs in the neighboring grains. This is reasonable since grains generally have different orientations on both sides of GBs and it is difficult for dislocations in one grain to glide to the neighboring grains directly. Dislocations are usually and firstly blocked by GBs during deformation, and with the increase in the number of blocked dislocations, a fore stress would be generated, which would induce the initiation of other dislocations from the GBs in the neighboring grains. Similar phenomenon has been reported in literature [34].

SE imaging and EBSD technique were used to deeply investigate the microstructural evolutions of the deformed 800AC and 950AC samples. Figures 7(a, b) reveal an SE image and the corresponding EBSD map in 800AC sample compressed by 6%. Lots of slip traces are detected on the surface of the sample and they are nearly parallel to each other in the $\beta$ matrix. When the slip trace crosses the spherical $\alpha$ particle, its orientation may change, as shown in Particle 2 in Fig. 7(a). Figure 8 illustrates local slip traces and pole figures

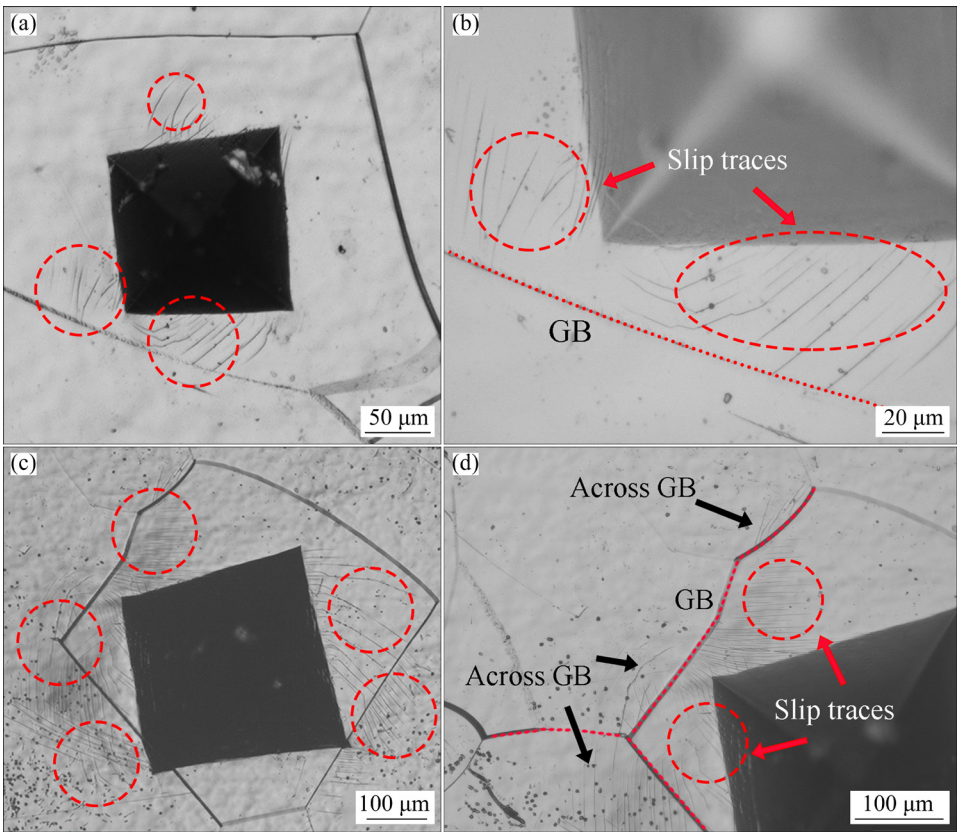


**Fig. 6** OM images (a, c) showing slip traces around two different pits generated by hardness tester in 950AC sample at loading forces of 50 N (a) and 300 N (c), and enlarged images (b, d) of areas immediately adjacent to pits in (a) and (c), respectively

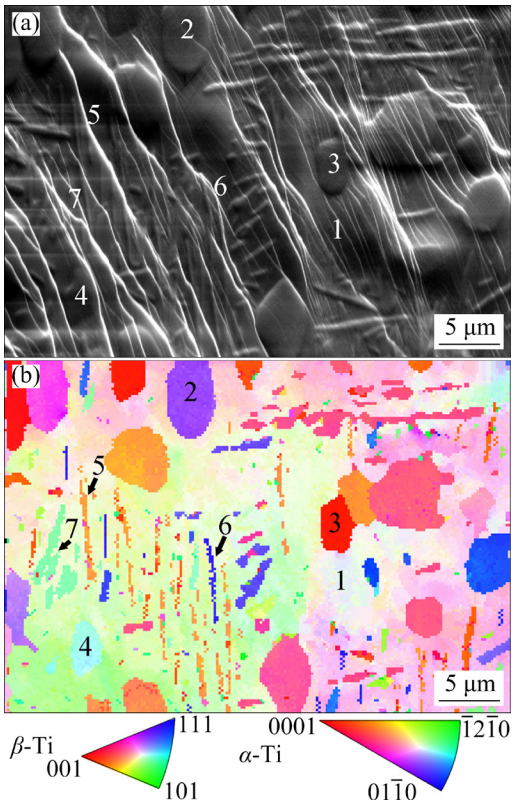


**Fig. 7** SE image showing slip traces in deformed 800AC sample (a) and corresponding EBSD image (b) (Numbers 1 to 7 mark seven different regions. Region 1 is $\beta$ matrix, Regions 2 to 4 are spherical $\alpha$ particles, and Regions 5 to 7 are plate-like $\alpha$ particles)

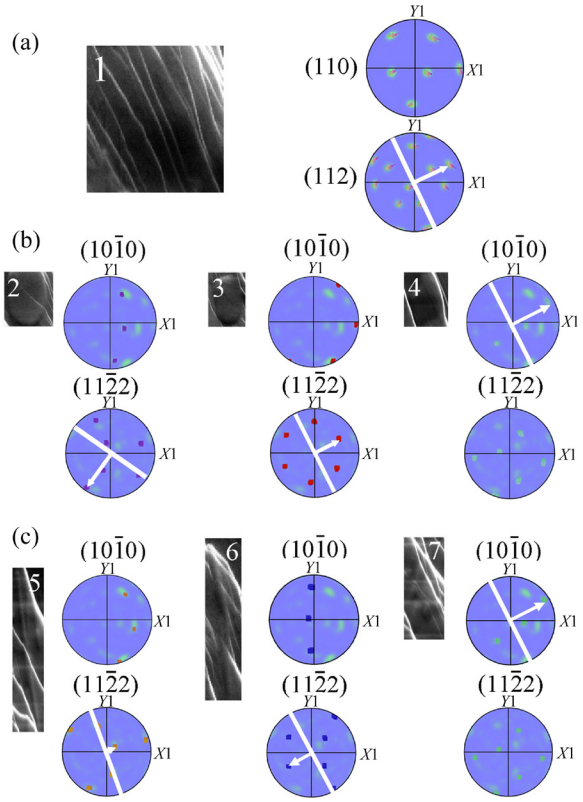


**Fig. 8** Localized slip traces in seven different regions in Fig. 7 and their corresponding pole figures illustrating method used to determine most likely activated slip system in these regions (The line on the pole figures corresponding to the slip trace): (a) $\beta$ matrix; (b) Spherical $\alpha$ particles; (c) Plate-like $\alpha$ particles

in seven different regions, as marked by numbers 1 to 7 in Fig. 7(a). The region in Fig. 8(a) comes from the $\beta$ matrix. Combining the orientation of slip traces and corresponding pole figures, the slip plane of the associated dislocations can be determined to be $(112)_\beta$. As the most closely packed direction within $(112)_\beta$ plane is $[11\bar{1}]_\beta$, the slip system could be speculated to be $(112)_\beta[11\bar{1}]_\beta$. According to our observations in five different regions of the $\beta$ matrix, the activated slip system is always $(112)_\beta[11\bar{1}]_\beta$ in the $\beta$ matrix. The $(112)_\beta\langle 11\bar{1}\rangle_\beta$ is the secondary preferred slip system in BCC materials, and the easiest slip system to activate is $(110)_\beta\langle 11\bar{1}\rangle_\beta$ [36,37]. The reason for the absence of $\{110\}_\beta\langle 11\bar{1}\rangle_\beta$ slip system might be that the combination of Al, Mo, Cr and Fe alloying elements increases its critical resolved shear stress (CRSS) or changes its dislocation core structure [38], resulting in its activation being more difficult than that of $\{112\}_\beta\langle 11\bar{1}\rangle_\beta$ slip system in the 800AC sample.

Figure 8(b) shows local slip traces and the corresponding pole figures of three spherical $\alpha$ particles in Fig. 7(a). Similar analysis reveals that the slip systems in Particles 2 and 3 are both $(11\bar{2}2)_\alpha[11\bar{2}3]_\alpha$ and the slip system in Particle 4 is $(10\bar{1}0)_\alpha[1\bar{2}10]_\alpha$. In the present study, eight spherical $\alpha$ particles were investigated, and $(11\bar{2}2)_\alpha[11\bar{2}3]_\alpha$ slip system was detected in five of them and $(10\bar{1}0)_\alpha[1\bar{2}10]_\alpha$ slip system was observed in the rest three. According to our observations, the slip traces were not only detected in the spherical $\alpha$ particles, but also observed in the plate-like $\alpha$ particles. Figure 8(c) shows slip traces and the corresponding pole figures of three plate-like $\alpha$ particles. Similarly, the slip systems in Plates 5 and 6 are both $(11\bar{2}2)_\alpha[11\bar{2}3]_\alpha$ and the slip system in Plate 7 is $(10\bar{1}0)_\alpha[1\bar{2}10]_\alpha$. Also, eight $\alpha$ plates were analyzed in this study. $(11\bar{2}2)_\alpha[11\bar{2}3]_\alpha$ slip system occurs in five of them and $(10\bar{1}0)_\alpha[1\bar{2}10]_\alpha$ slip system occurs in the rest

three. Therefore, selection of slip system in $\alpha$ phase seems to be irrespective of the morphology of $\alpha$ particles. Since there are six equivalent $\{11\bar{2}2\}_\alpha\langle 11\bar{2}3\rangle_\alpha$ slip systems and three equivalent $\{10\bar{1}0\}_\alpha\langle 1\bar{2}10\rangle_\alpha$ slip systems in the $\alpha$ lattice with an HCP structure [39], the occurrence of $\{11\bar{2}2\}_\alpha\langle 11\bar{2}3\rangle_\alpha$ slip systems in the $\alpha$ particles would coordinate the plastic deformation better. Considering that $\{10\bar{1}0\}_\alpha\langle 1\bar{2}10\rangle_\alpha$ slip system is generally the most common one, higher observed frequency of $\{11\bar{2}2\}_\alpha\langle 11\bar{2}3\rangle_\alpha$ slip system may be attributed to the effects of alloying elements in the $\alpha$ phase.

Figures 9(a) and (b) show SE image and corresponding EBSD map on a polished surface of 950AC specimen compressed by 6%. Five $\beta$ grains are observed in the image. By analyzing the slip traces and pole figure of Grain 1, the slip plane of dislocations in the grain can be determined to be $(110)_\beta$ and thus the slip system is $(110)_\beta[1\bar{1}1]_\beta$ or $(110)_\beta[\bar{1}11]_\beta$. In addition to the slip traces, many narrow bands can be observed in Grain 1 and they are parallel to each other. Figure 10(a) shows an enlarged SE image of these bands. They have a width of 2−5 μm, and the EBSD map indicates that they are $\alpha''$ phase. As there is no $\alpha''$ phase observed in the solution-treated 950AC sample, these $\alpha''$ phases are suggested to be generated by martensite transformation, i.e., the stress-induced martensite transformation during deformation. In addition, there are some deformed grains that do not include $\alpha''$ martensite but include two kinds of different slip traces, such as Grain 2 in Fig. 9. Careful analyses reveal that the two different slip traces correspond to two different slip systems: $\{110\}_\beta\langle 1\bar{1}1\rangle_\beta$ and $\{112\}_\beta\langle 1\bar{1}1\rangle_\beta$, respectively. Since these two slip systems have the same Burgers vectors, cross-slip of dislocation may occur from one to the other. $\alpha''$ martensite is only detected in a few $\beta$ grains and the deformed microstructure is dominated by the dislocation slipping in the deformed sample according to our observations. Since dislocation slipping in single $\beta$ phase generally arises a low strain hardening rate [40], the 950AC sample has a relatively low strain hardening rate, as shown in Fig. 3(b).

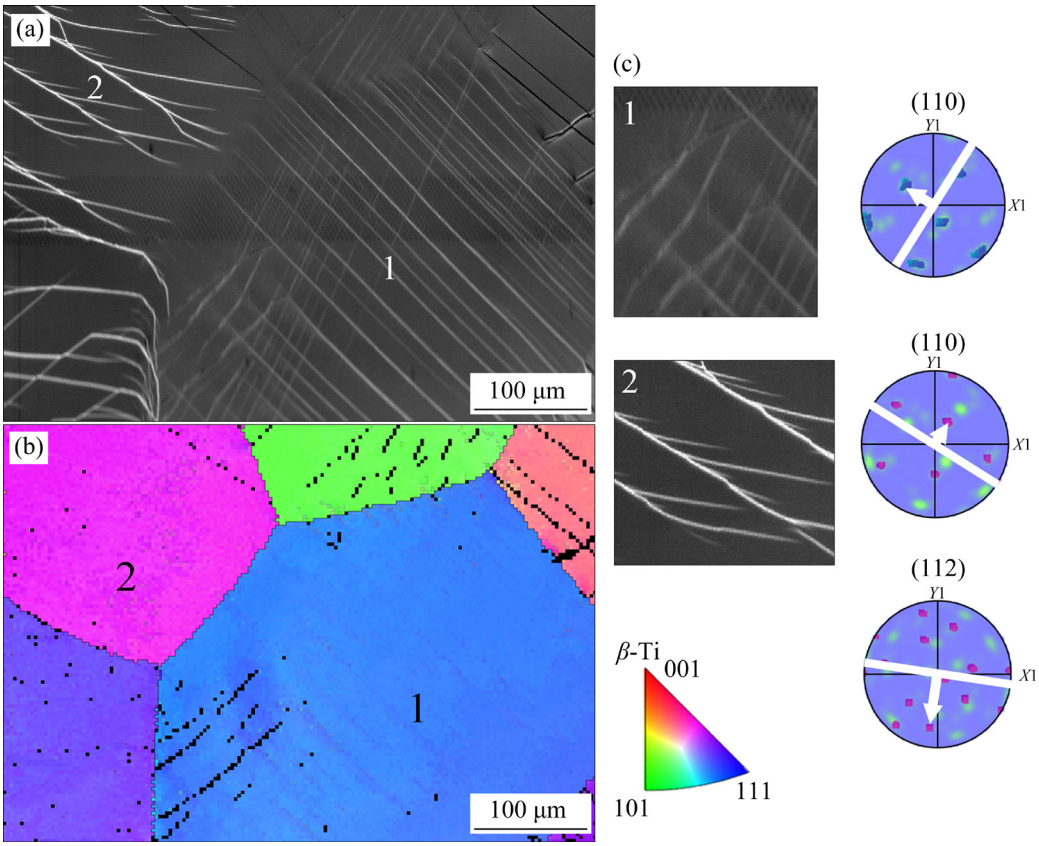


**Fig. 9** SE image showing slip traces in deformed 950AC sample (a), corresponding EBSD image (b), and localized slip traces and corresponding pole figures in Grains 1 and 2, showing most probable slip planes of dislocations in two grains (c)

Kernel average misorientation (KAM) map based on EBSD data was used to analyze the dislocation distribution in the deformed 800AC and 950AC samples. Figure 11(a) shows the KAM map of $\alpha$ phase in the deformed 800AC sample. Relatively large misorientation was detected in both spherical and plate-like $\alpha$ phases, implying that high number density dislocation exists in them. This indicates the occurrence of plastic deformation in the $\alpha$ phase, which is consistent with the results in Figs. 7 and 8. Figure 11(b) shows the KAM map of the $\beta$ matrix in the deformed 800AC sample. Expectedly, large misorientation caused by high number density dislocation can be observed, but the distribution of misorientation is non-uniform. The largest misorientation distributes at the interfaces between the $\alpha$ and $\beta$ phases, and the misorientations in the regions away from $\alpha$ phase are relatively low, as marked by red circles. This is reasonable since $\alpha/\beta$ interfaces can hinder the movement of dislocations during deformation and thus lots of dislocations could be stored adjacent to the interfaces after deformation.

Figure 12(a) shows a corresponding KAM map of Fig. 9(b) in the deformed 950AC sample. Grain 1 shows a uniform misorientation and its

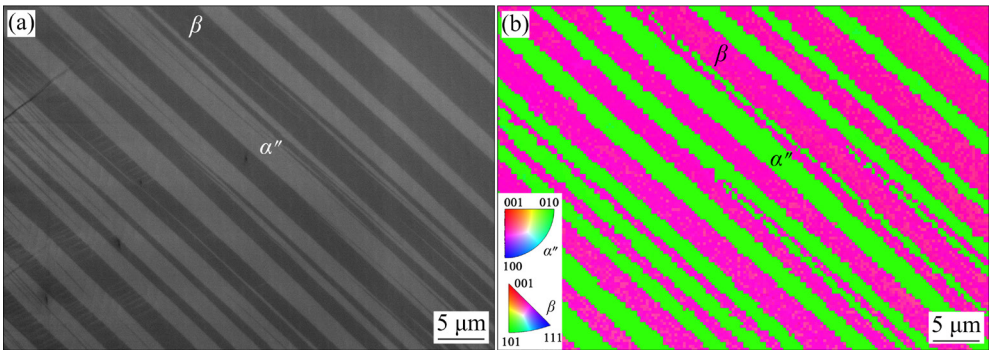


**Fig. 10** SE image (a) and EBSD map (b) showing presence of $\alpha''$ martensite in deformed 950AC sample

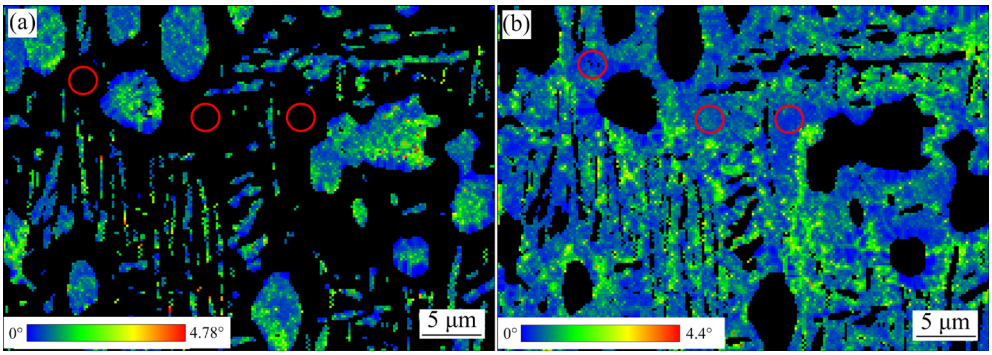


**Fig. 11** KAM images showing misorientation distribution in $\alpha$ phase (a) and $\beta$ phase (b) in deformed 800AC sample

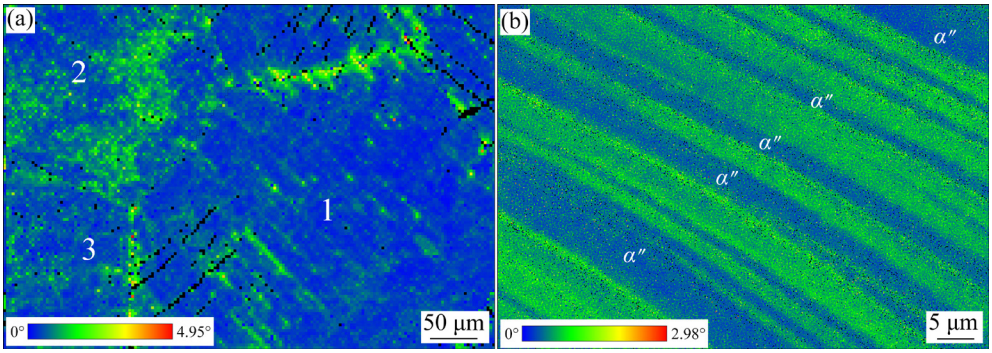


**Fig. 12** Low-magnification KAM image showing misorientation distribution in deformed 950AC sample (a) and high-magnification KAM image (b) of Grain 1 in (a)

value is relatively low, while Grain 2 shows a larger misorientation but its distribution is non-uniform. As $\alpha''$ martensite transformation occurs in Grain 1 and only dislocation slip occurs in Grain 2, it can be speculated that martensite transformation results in a homogeneously plastic deformation. This is further demonstrated in a high magnification KAM map of Grain 1, as shown in Fig. 12(b). The misorientation in $\alpha''$ martensite is low and the misorientation in the $\beta$ lamellae between $\alpha''$ martensite is very uniform. In addition, some grains without $\alpha''$ martensite present low and uniform misorientation, as exemplified by Grain 3 in Fig. 12(a). According to our calculations of Schmid factors, the Schmid factors for $\{110\}_\beta\langle 1\bar{1}1\rangle_\beta$ and $\{112\}_\beta\langle 1\bar{1}1\rangle_\beta$ slip systems in Grain 3 are 0.46 and 0.45, respectively, which are smaller than 0.49 and 0.47 for the two slip systems in Grain 2. This implies that the activation of these two slip systems is more difficult in grain. In other words, the orientation of the grain is not suitable for dislocation slipping due to the smaller Schmid factors. Moreover, the largest misorientation in the deformed 950AC sample is detected at GBs, as shown in Fig. 12(a). This is expected as GBs act as the dislocation barriers and can lead to the pile-up of dislocations, which is consistent with the results in Fig. 6.

Based on the above experimental results, the tensile properties of the 800AC and 950AC samples can be understood. The superior strength−ductility synergy of the 800AC sample is attributed to the existence of spherical and plate-like $\alpha$ phases. The interphase boundaries could impede the dislocation movement at the early stage of deformation (Fig. 5(b)), giving rise to the high strength. With the increase in the amount of deformation, the dislocation could cross the interphase boundaries and cause the plastic deformation in $\alpha$ phases (Fig. 5(d)), which would relief the stress concentration and inhibit the initiation of crack at interphase boundaries, and then result in good ductility of the alloy [41]. For the 950AC specimen, two kinds of slip systems and stress-induced $\alpha''$ martensite transformation contribute concurrently to its good ductility. But once the crack forms within the sample, it would propagate quickly along the boundaries of the martensite, leading to the occurrence of quasi-cleavage fracture of the sample (Fig. 4(d)).

## 4 Conclusions

(1) The 800AC sample with a duplex microstructure has a tensile yield strength (TYS) of 886 MPa, an ultimate tensile strength (UTS) of 1075 MPa, and an elongation of 21.5%. The 950AC sample with a single $\beta$ phase microstructure has a TYS of 760 MPa, an UTS of 866 MPa and an elongation of 22.5%.

(2) The fracture microstructure of the 800AC sample consists of dimples and its fracture mode is ductile fracture. The fracture microstructure of the 950AC sample is dominated by torn edges and cleavage faces, although a few shallow dimples are occasionally observed, and the fracture mode of the alloy is quasi-cleavage fracture.

(3) The deformation mode of the 800AC sample is dislocation slipping. It can occur not only in the $\beta$ matrix but also in the spherical and plate-like $\alpha$ particles. The slip system in $\beta$ matrix is $\{112\}_\beta\langle 1\bar{1}1\rangle_\beta$. The slip systems in the spherical and plate-like $\alpha$ particles are the same, and they are $\{11\bar{2}2\}_\alpha\langle 11\bar{2}\bar{3}\rangle_\alpha$ and $\{10\bar{1}0\}_\alpha\langle 1\bar{2}10\rangle_\alpha$.

(4) The deformation mode of the 950AC sample includes dislocation slipping and stress-induced $\alpha''$ martensite transformation, and the slip systems include $\{110\}_\beta\langle 1\bar{1}1\rangle_\beta$ and $\{112\}_\beta\langle 1\bar{1}1\rangle_\beta$. The concurrence of dislocation slipping and stress-induced martensite transformation is the origin of good ductility of the 950AC sample.

## Acknowledgments

This work was financially supported by the National Natural Science Foundation of China (No. 51828102).

## References

[1] PRAKASH K R, DEVARAJ A. A review of metastable beta titanium alloys [J]. Metals, 2018, 8: 506.

[2] KANG Li-mei, YANG Chao. A review on high-strength titanium alloys: microstructure, strengthening, and properties [J]. Advanced Engineering Materials, 2019, 21: 1801359.

[3] KAUR M, SINGH K. Review on titanium and titanium based alloys as biomaterials for orthopaedic applications [J]. Materials Science and Engineering C, 2019, 102: 844−862.

[4] HUSSEIN M, ADESINA A Y, KUMAR M, AZEEM M, SOROUR A, AL-AQEELI N. Improvement of in vitro corrosion, wear, and mechanical properties of newly developed Ti alloy by thermal treatment for dental

applications [J]. Transactions of Nonferrous Metals Society of China, 2021, 31: 952−966.

[5] HUANG Chao-wen, ZHAO Yong-qing, XIN She-wei, ZHOU Wei, LI Qian, ZENG Wei-dong. Effect of microstructure on tensile properties of Ti−5Al−5Mo−5V−3Cr−1Zr alloy [J]. Journal of Alloys and Compounds, 2017, 693: 582−591.

[6] ZHU Cheng-peng, PENG Gen-shen, LIN Yong-cheng, ZHANG Xiao-yong, LIU Chao-qiang, ZHOU Ke-chao. Effects of Mo and Cr contents on microstructures and mechanical properties of near $\beta$-Ti alloy [J]. Materials Science and Engineering A, 2021, 825: 141882.

[7] DU Zhao-xin, MA Yan, LIU Fei, ZHAO Xue-ping, CHEN Yan-fei, LI Guo-wei, LIU Guo-long, CHEN Yu-yong. Improving mechanical properties of near beta titanium alloy by high-low duplex aging [J]. Materials Science and Engineering A, 2019, 754: 702−707.

[8] HASHMI M L, WADOOD A. Microstructural, mechanical and shape memory characterizations of Ti−Mo−Sn alloys [J]. Transactions of Nonferrous Metals Society of China, 2020, 30: 688−700.

[9] MANTRI S A, CHOUDHURI D, ALAM T, VISWANATHAN G B, SOSA J M, FRASER H L, BANERJEE R. Tuning the scale of $\alpha$ precipitates in $\beta$-titanium alloys for achieving high strength [J]. Scripta Materialia, 2018, 154: 139−144.

[10] ZHAO Zhuang, CHEN Jing, TAN Hua, ZHANG Guo-hao, LIN Xin, HUANG Wei-dong. Achieving superior ductility for laser solid formed extra low interstitial Ti−6Al−4V titanium alloy through equiaxial alpha microstructure [J]. Scripta Materialia, 2018, 146: 187−191.

[11] SADEGHPOUR S, ABBASI S M, MORAKABATI M, BRUSCHI S. Correlation between alpha phase morphology and tensile properties of a new beta titanium alloy [J]. Materials & Design, 2017, 121: 24−35.

[12] JIANG B Z, EMURA S, TSUCHIYA K. Improvement of ductility in Ti−5Al−5Mo−5V−3Cr alloy by network-like precipitation of blocky $\alpha$ phase [J]. Materials Science and Engineering A, 2018, 722: 129−135.

[13] MANTRI S A, CHOUDHURI D, ALAM T, AGEH V, SUN F, PRIMA F, BANERJEE R. Change in the deformation mode resulting from beta-omega compositional partitioning in a TiMo alloy: Room versus elevated temperature [J]. Scripta Materialia, 2017, 130: 69−73.

[14] LI Yang-huan-zi, OU Xiao-qin, NI Song, SONG Min. Deformation behaviors of a hot rolled near-$\beta$ Ti−5Al−5Mo−5V−1Cr−1Fe alloy [J]. Materials Science and Engineering A, 2019, 742: 390−399.

[15] LI Yang-huan-zi, NI Song, LIU Yong, SONG Min. Phase transition induced high strength and large ductility of a hot rolled near $\beta$ Ti−5Al−5Mo−5V−1Cr−1Fe alloy [J]. Scripta Materialia, 2019, 170: 34−37.

[16] REN Lei, XIAO Wen-long, KENT D, WAN Min, MA Chao-li, ZHOU Lian. Simultaneously enhanced strength and ductility in a metastable $\beta$-Ti alloy by stress-induced hierarchical twin structure [J]. Scripta Materialia, 2020, 184: 6−11.

[17] NIE Hui-hui, ZHENG Liu-wei, KANG Xiao-ping, HAO Xin-wei, LI Xian-rong, LIANG Wei. In-situ investigation of deformation behavior and fracture forms of Ti/Al/Mg/Al/Ti laminates [J]. Transactions of Nonferrous Metals Society of China, 2021, 31: 1656−1664.

[18] CHEN Kui-wai, PAN Su-ping, LIU Hui-qun, JIANG Yong. Effect of $\alpha$ phase morphology on fatigue crack growth behavior of Ti−5Al−5Mo−5V−1Cr−1Fe alloy [J]. Transactions of Nonferrous Metals Society of China, 2020, 30: 2459−2471.

[19] CHEN Wei, LV Ya-ping, WANG Han-de, ZHANG Xiao-yong, CHEN Chao, LIN Yong-cheng, ZHOU Ke-chao. On the $\{10\bar{1}1\}$ twin-accommodated mechanisms in equiaxed near $\beta$-Ti alloys operating by unidirectional and cross rolling [J]. Materials Science and Engineering A, 2020, 769: 138516.

[20] SUN F, ZHANG J Y, MARTELEUR M, GLORIANT T, VERMAUT P, LAILLÉ D, CASTANY P, CURFS C, JACQUES P J, PRIMA F. Investigation of early stage deformation mechanisms in a metastable $\beta$ titanium alloy showing combined twinning-induced plasticity and transformation-induced plasticity effects [J]. Acta Materialia, 2013, 61: 6406−6417.

[21] ZHU Yu-man, ZHU Su-ming, NIE Jian-feng. Atomic-scale study of {112} twin boundary structure in a $\beta$-Ti alloy [J]. Philosophical Magazine Letters, 2016, 96: 280−285.

[22] MARTELEUR M, SUN F, GLORIANT T, VERMAUT P, JACQUES P J, PRIMA F. On the design of new $\beta$-metastable titanium alloys with improved work hardening rate thanks to simultaneous TRIP and TWIP effects [J]. Scripta Materialia, 2012, 66: 749−752.

[23] POLMEAR I, STJOHN D, NIE Jian-feng, QIAN Ma. Titanium alloys [M]. Boston: Butterworth-Heinemann, 2017: 369−460.

[24] CHEN Bin, SUN Wei. Transitional structure of $\{332\}\langle 113\rangle_\beta$ twin boundary in a deformed metastable $\beta$-type Ti-Nb-based alloy, revealed by atomic resolution electron microscopy [J]. Scripta Materialia, 2018, 150: 115−119.

[25] ZHAO G H, XU X, DYE D, RIVERA-DÍAZ-DEL-CASTILLO P E J. Microstructural evolution and strain-hardening in TWIP Ti alloys [J]. Acta Materialia, 2020, 183: 155−164.

[26] GAO Jun-heng, HUANG Yu-he, GUAN Di-kai, KNOWLES A J, MA Le, DYE D, RAINFORTH W M. Deformation mechanisms in a metastable beta titanium twinning induced plasticity alloy with high yield strength and high strain hardening rate [J]. Acta Materialia, 2018, 152: 301−314.

[27] AHMED M, WEXLER D, CASILLAS G, SAVVAKIN D G, PERELOMA E V. Strain rate dependence of deformation-induced transformation and twinning in a metastable titanium alloy [J]. Acta Materialia, 2016, 104: 190−200.

[28] TOBE H, KIM H Y, INAMURA T, HOSODA H, MIYAZAKI S. Origin of {332} twinning in metastable $\beta$-Ti alloys [J]. Acta Materialia, 2014, 64: 345−355.

[29] ZHANG J, TASAN C C, LAI M J, DIPPEL A C, RAABE D. Complexion-mediated martensitic phase transformation in titanium [J]. Nature Communications, 2017, 8: 14210.

[30] WANG X L, LI L, MEI W, WANG W L, SUN J. Dependence of stress-induced omega transition and

mechanical twinning on phase stability in metastable β Ti−V alloys [J]. Materials Characterization, 2015, 107: 149−155.
[31] AHMED M, WEXLER D, CASILLAS G, IVASISHIN O M, PERELOMA E V. The influence of β phase stability on deformation mode and compressive mechanical properties of Ti−10V−3Fe−3Al alloy [J]. Acta Materialia, 2015, 84: 124−135.
[32] CEPEDA-JIMÉNEZ C M, MOLINA-ALDAREGUIA J M, PÉREZ-PRADO M T. Effect of grain size on slip activity in pure magnesium polycrystals [J]. Acta Materialia, 2015, 84: 443−456.
[33] ZHAO Ling-yu, XIN Yun-chang, GUO Fei-long, YU Hui-hui, LIU Qing. A new annealing hardening mechanism in pre-twinned Mg−3Al−1Zn alloy [J]. Materials Science and Engineering A, 2016, 654: 344−351.
[34] YU Hui-hui, LI Chang-zheng, XIN Yun-chang, CHAPUIS A, HUANG Xiao-xu, LIU Qing. The mechanism for the high dependence of the Hall−Petch slope for twinning/slip on texture in Mg alloys [J]. Acta Materialia, 2017, 128: 313−326.
[35] NG H P, DOUGUET E, BETTLES C J, MUDDLE B C. Age-hardening behaviour of two metastable beta-titanium alloys [J]. Materials Science and Engineering A, 2010, 527: 7017−7026.
[36] HULL D, BACON D J. Movement of dislocations [M]. 5th ed. Amsterdam: Elsevier, 2011.
[37] CAO Yang, NI Song, LIAO Xiao-zhou, SONG Min, ZHU Yun-tian. Structural evolutions of metallic materials processed by severe plastic deformation [J]. Materials Science and Engineering R, 2018, 133: 1−59.
[38] VITEK V. Structure of dislocation cores in metallic materials and its impact on their plastic behaviour [J]. Progress in Materials Science, 1992, 36: 1−27.
[39] LÜTJERING G, WILLIAMS J C. Titanium [M]. 2nd ed. Berlin: Springer, 2007.
[40] XUE Q, MA Y J, LEI J F, YANG R, WANG C. Mechanical properties and deformation mechanisms of Ti−3Al−5Mo−4.5V alloy with varied β phase stability [J]. Journal of Materials Science & Technology, 2018, 34: 2507−2514.
[41] XU Jian-wei, ZENG Wei-dong, ZHOU Da-di, HE Sheng-tong, JIA Run-chen. Evolution of coordination between α and β phases for two-phase titanium alloy during hot working [J]. Transactions of Nonferrous Metals Society of China, 2021, 31: 3428−3438.

# 双态与单相 Ti−5Al−5Mo−1Fe−1Cr 合金的力学性能及变形行为

刘超强[1]，谢宗瑜[1]，张晓泳[1]，严红革[2]，周科朝[1]，宋 旼[1]

1. 中南大学 粉末冶金国家重点实验室，长沙 410083；
2. 湖南大学 材料科学与工程学院，长沙 410082

**摘 要**：为了阐明具有双态和单相组织 Ti−5Al−5Mo−1Fe−1Cr(质量分数，%)合金的力学性能及变形行为，系统研究具有这两种组织合金的力学性能和变形模式。研究结果表明：双态组织合金的拉伸屈服强度为 886 MPa，极限抗拉强度为 1075 MPa，伸长率为 21.5%；单相(β)组织合金的强度稍低于双态合金的，但其伸长率与双态合金的类似。双态合金在拉伸过程中具有韧性断裂的特征，其主要变形模式为位错滑移，位错滑移可发生于 β 基体和球/片状 α 相，β 基体中的滑移系为 $\{112\}_{\beta}\langle 11\bar{1}\rangle_{\beta}$，α 相中的滑移系为 $\{11\bar{2}2\}_{\alpha}\langle 11\bar{2}\bar{3}\rangle_{\alpha}$ 和 $\{10\bar{1}0\}_{\alpha}\langle 1\bar{2}10\rangle_{\alpha}$。相对地，单相合金具有解理断裂特征，变形模式包括位错滑移和应力诱导 α″马氏体相变，其滑移系包括 $\{110\}_{\beta}\langle 1\bar{1}1\rangle_{\beta}$ 和 $\{112\}_{\beta}\langle 11\bar{1}\rangle_{\beta}$。

**关键词**：近 β 钛合金；力学性能；变形行为；位错滑移；应力诱导马氏体相变

**(Edited by Wei-ping CHEN)**